



Wear-Resistant Fe-Based Metallic Glass- Al_2O_3 Composite Coatings Produced by Detonation Spraying

Ivanna D. Kuchumova^{1,2} · Nina Yu. Cherkasova² · Igor S. Batraev¹ · Vladislav S. Shikalov³ · Arina V. Ukhina⁴ · Guilherme Yuuki Koga⁵ · Alberto Moreira Jorge Jr.^{5,6,7}

Submitted: 11 June 2021 / in revised form: 29 November 2021 / Accepted: 29 November 2021 / Published online: 19 January 2022
© ASM International 2021

Abstract Al_2O_3 particle-modified $\text{Fe}_{66}\text{Cr}_{10}\text{Nb}_5\text{B}_{19}$ metallic glass matrix coatings were deposited on carbon steel substrates by detonation spraying of the corresponding powder mixtures. The microstructure, mechanical and tribological properties of the coatings were investigated. In the microstructure of the coatings, the Al_2O_3 particles were located between the layers of the $\text{Fe}_{66}\text{Cr}_{10}\text{Nb}_5\text{B}_{19}$ amorphous alloy. The bonding strength between the substrate and composite coatings was ~ 130 MPa. The wear

behavior of the coatings was studied under dry linearly reciprocating conditions in a ball-on-flat mode using a WC-6Co ball as a counterbody. It was found that the friction coefficients of the Al_2O_3 -free coating and composite coatings were close to each other and varied in the range of 0.64–0.70. The specific wear rate of the coatings modified with 1.5 and 4 vol.% of Al_2O_3 was 2.5×10^{-5} and $3.1 \times 10^{-5} \text{ mm}^3 \text{ N}^{-1} \text{ m}^{-1}$, respectively, which is about one-fifth of the specific wear rate of stainless steel. It was suggested that the dominating wear mechanisms of the $\text{Fe}_{66}\text{Cr}_{10}\text{Nb}_5\text{B}_{19}$ - Al_2O_3 composite coatings are fatigue and abrasion wear.

This article is part of a special topical focus in the Journal of Thermal Spray Technology on High Entropy Alloy and Bulk Metallic Glass Coatings. The issue was organized by Dr. Andrew S.M. Ang, Swinburne University of Technology; Prof. B.S. Murty, Indian Institute of Technology Hyderabad; Distinguished Prof. Jien-Wei Yeh, National Tsing Hua University; Prof. Paul Munroe, University of New South Wales; Distinguished Prof. Christopher C. Berndt, Swinburne University of Technology. The issue organizers were mentored by Emeritus Prof. S. Ranganathan, Indian Institute of Sciences.

Keywords bulk metallic glass · coating · composite · steel · thermal spraying · wear

✉ Ivanna D. Kuchumova
ivannakz@mail.ru

¹ Lavrentyev Institute of Hydrodynamics SB RAS, 15, Lavrentyev Ave., Novosibirsk, Russia 630090

² Novosibirsk State Technical University, 20, K. Marx Ave., Novosibirsk, Russia 630073

³ Khristianovich Institute of Theoretical and Applied Mechanics SB RAS, 4/1, Institutskaya St., Novosibirsk, Russia 630090

⁴ Institute of Solid State Chemistry and Mechanochemistry SB RAS, 18, Kutateladze St., Novosibirsk, Russia 630128

⁵ Department of Materials Science and Engineering, Federal University of São Carlos, Via Washington Luiz, km 235, São Carlos, SP 13565-905, Brazil

⁶ CNRS, Grenoble INP, LEPMI, Univ. Grenoble Alpes, Univ. Savoie Mont Blanc, 38000 Grenoble, France

⁷ CNRS, Grenoble INP, SIMAP, Univ. Grenoble Alpes, 38000 Grenoble, France

Introduction

Metallic glasses possess an excellent combination of properties, which include high mechanical strength, high wear resistance and high corrosion resistance. These properties originate from a lack of the long-range order in the atomic structure of the glasses (Ref 1-3). Fe-based metallic glasses are promising materials for developing protective coatings to withstand corrosive environments and wear (Ref 4-6). Recently, efforts have been made to produce Fe-based metallic glass coatings by thermal spraying, such as, high-velocity oxy-fuel (HVOF) (Ref 7), plasma (Ref 8), detonation (Ref 9) spraying, as well as by laser cladding (Ref 10). The advantages of detonation spraying over other deposition techniques are a high productivity and a pulse nature of the deposition process. Xie et al. (Ref 11) showed that detonation coatings obtained from the $\text{Fe}_{48}\text{Mo}_{14}\text{Cr}_{15}\text{Y}_2\text{C}_{15}\text{B}_6$ powder provide better mechanical properties than coatings produced by plasma spraying and HVOF. In our studies (Ref 12, 13), parameters of the detonation spraying process were determined for depositing $\text{Fe}_{66}\text{Cr}_{10}\text{Nb}_5\text{B}_{19}$ coatings. Dense coatings with amorphous structure and high bonding strength to steel substrates were obtained.

Due to a limited ductility, metallic glass coatings can exhibit low fracture resistance and toughness, which reduce the scope of their application in industry (Ref 14). Laminated structures or metallic glass matrix composites with a crystalline second phase can be designed to increase the fracture toughness of the coatings. The essence of the first approach is to form multilayer structures with alternating amorphous and crystalline layers. As reported by Zhang et al. (Ref 15), Fe-based amorphous alloy/NiCrAl multilayer structure possess a much higher toughness than the monolithic amorphous alloy coating. The second approach is to form a coating from a mixture of a Fe-based alloy and second-phase particles. Fe-based amorphous alloy coatings containing 8 vol.% of stainless steel particles showed an improved fracture resistance relative to the monolithic amorphous coatings (Ref 16). It was shown that the stainless steel particles could effectively absorb the fracture energy. However, the addition of the stainless steel powder decreases the corrosion resistance of the composite coatings, as pitting corrosion preferentially occurs at the interface between the crystalline particles and the amorphous matrix (Ref 17). In-situ crystallization resulting in the formation of second-phase particles in the coatings upon deposition is an alternative route (Ref 18, 19). However, the forming crystals can become enriched in Cr, creating Cr-depleted interfaces, which suffer localized corrosion in case of excessive crystallization (Ref 20, 21).

The tribological properties and corrosion resistance of amorphous alloy coatings can be considerably influenced by the presence of embedded particles, such as particles of amorphous carbon (Ref 22), WC-Co alloys (Ref 23), or nitrides (Ref 24). The amorphous matrix ensures a high corrosion resistance of the coatings. The crystalline particles of ceramic nature may increase the wear resistance of the amorphous coatings.

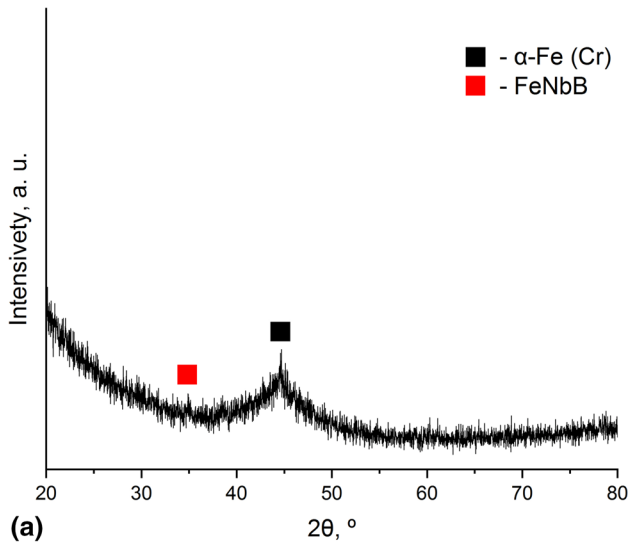
Yoon et al. (Ref 25) reported the properties of Fe-based amorphous alloy- B_4C composite coatings. As the B_4C content in the composite coatings increases, their wear resistance tends to improve relative to that of B_4C -free coatings. It was shown that boron carbide particles play an important role, acting as solid “lubricants” during the sliding friction wear tests. As shown in ref. (Ref 26), the modification of Fe-based amorphous alloy coatings with ceramic particles does not usually affect the corrosion resistance of the coatings, as no galvanic coupling occurs. It should also be noted that the introduction of ceramic particles into an amorphous alloy matrix does not lead to the formation of Cr-depleted interfaces. The addition of Al_2O_3 particles into Fe-based amorphous alloy coatings improves the toughness of the material owing to crack blockage and deflection by the particles, and the microcrack formation inside the Al_2O_3 particles (Ref 27). The literature overview shows that the formation mechanisms and microstructural features of Fe-based amorphous alloy composite coatings have not been extensively studied. Further research in this area would allow developing coatings with novel sets of properties.

In the present study, $\text{Fe}_{66}\text{Cr}_{10}\text{Nb}_5\text{B}_{19}$ metallic glass coatings modified with Al_2O_3 particles were fabricated by detonation spraying. The effect of the Al_2O_3 content (in the 20–60 wt.% range) in the initial powder mixture on the phase composition and microstructure of the composite coatings was investigated by X-ray diffraction (XRD) and scanning electron microscopy (SEM). Vickers hardness, bonding strength (pin test method) and tribological behavior (reciprocating ball-on-flat sliding test) of the composite coatings were examined. The wear resistance of the composite coatings was compared with that of Al_2O_3 -free amorphous alloy coatings and stainless steel.

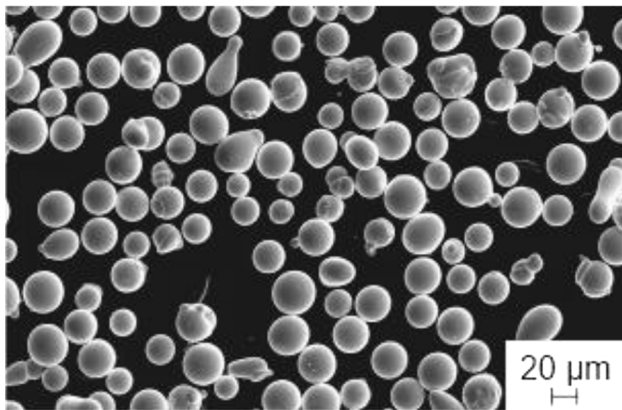
Materials and Methods

The $\text{Fe}_{66}\text{Cr}_{10}\text{Nb}_5\text{B}_{19}$ powder was obtained by gas atomization using a HERMIGA 75/5VI gas atomizer (Phoenix Scientific Industries Ltd., UK). The powder was sieved to separate the 20–40 μm fraction. The starting Al_2O_3 powder had a purity of > 99.5 wt.% and particles in the 20–45 μm range (GTV Wear Protection GmbH, Germany). The metallic glass powder was mixed with the

Al₂O₃ powder. The Al₂O₃ content in mixture was 20, 40 or 60 wt.%. The mixtures were prepared in a mortar; the duration of mixing was 15 min.



(a)



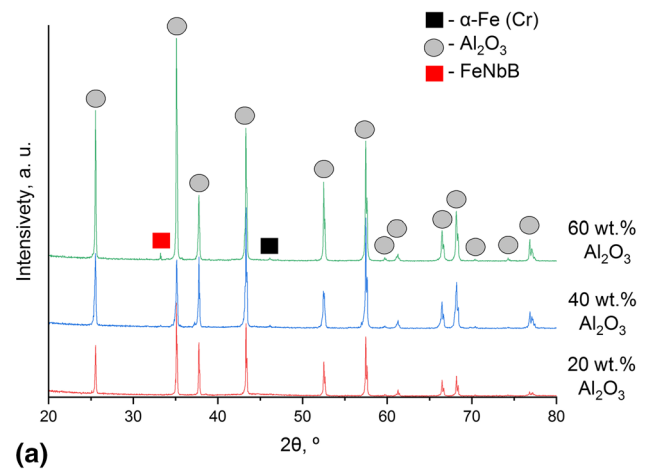
(b)



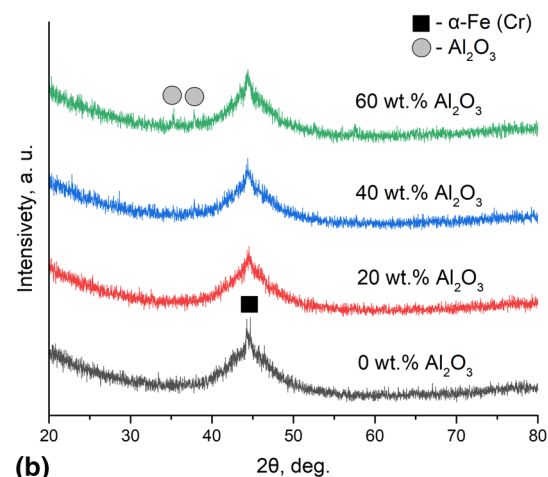
(c)

Fig. 1 Characteristics of the feedstock powders: (a) XRD pattern and (b) SEM image of the Fe₆₆Cr₁₀Nb₅B₁₉ powder; (c) SEM image of the Al₂O₃ powder. Micrographs were taken in the SE imaging mode

Detonation spraying of the powder mixtures was performed using a computer-controlled detonation spraying (CCDS2000) system (Ref 28). The barrel had a variable cross section (Ref 29). The total length of the barrel was 1000 mm. The diameter of the combustion chamber and the acceleration section was 20 and 16 mm, respectively. The spraying distance was 200 mm. Coatings were deposited at an O₂/C₂H₂ molar ratio of 1.1 and an explosive charge of 50%. (A fraction of the barrel volume was filled with the gas mixture.) Nitrogen was used as a carrier gas. Previous studies have shown that, under such conditions, spraying allows obtaining high-quality coatings in terms of the amorphous phase content, adhesion, porosity and hardness (Ref 12). The composite coatings were deposited on carbon steel substrates (carbon steel, Grade St3, GOST 380-2005, analog to ASTM A570). The thickness of the deposited coatings was 250–300 μm. Before spraying, the substrates were sandblasted to ensure better adhesion of the coatings. The temperatures and velocities of the particles at the exit of the barrel were



(a)



(b)

Fig. 2 XRD patterns of the feedstock powder mixtures (a) and coatings obtained by detonation spraying (b)

calculated using LIH software developed at Lavrentyev Institute of Hydrodynamics SB RAS (Ref 30, 31).

XRD analysis of the powders and coatings was carried out using a Bruker D8 ADVANCE diffractometer (Bruker AXS, Germany). The crystalline phase content of the starting $\text{Fe}_{66}\text{Cr}_{10}\text{Nb}_5\text{B}_{19}$ powder was determined by the Rietveld method using TOPAS 4.2 software (Bruker AXS, Germany). XRD patterns were taken from the polished surfaces of the coatings.

The morphology of the powders and microstructure of the coatings were studied by SEM in the secondary electron (SE) imaging mode using an EVO50 XVP microscope (Carl Zeiss, Germany) coupled with an energy-dispersive spectroscopy (EDS) X-Act system (Oxford Instruments, UK). The distribution of Al_2O_3 particles in the composite coatings was determined by elemental mapping.

The porosity of the coatings and the content of alumina particles in the coatings were determined using OLYMPUS Stream Image Analysis Software “Stream Essentials 1.9.1” (OLYMPUS, Japan). Optical images of the samples were recorded on an OLYMPUS GX-51 Optical Microscope (OLYMPUS, Japan). The fracture surface of the coatings was studied on a TM-1000 Tabletop microscope (Hitachi, Japan) in the back-scattered electron (BSE) imaging mode.

The hardness of the coatings was measured on polished cross sections using a Vickers hardness testing device (402MVD, Wolpert Wilson Instruments, Germany) under a load of 1 kg with a dwell time of 15 s. The average values of hardness were determined from 10 measurements.

The wear behavior of the coatings and stainless steel (grade 12Cr18Ni10Ti, GOST 2590-2006, analog to ASTM 321) was investigated by a standard test method for linearly reciprocating ball-on-flat sliding wear (ASTM G133-05) using a UMT-2 wear machine (Bruker Nano GmbH, Germany) (Ref 32). This test method uses a hard WC-6Co ball 6.35 mm in diameter. The ball was sliding against a flat specimen. Before the wear tests, the coatings and stainless steel surfaces were polished to a mirror finish. The ball and the sample were degreased with acetone and dried before testing to ensure nominal dry sliding conditions (40–60% relative humidity).

The normal load (25 N) was applied vertically downward through the ball against a flat coating mounted horizontally. The sliding speed was 5 mm s^{-1} , and the stroke length was 5 mm. The total sliding distance was 100 m. An analytical balance, with an accuracy of 0.1 mg, was used for weighing the coating samples before and after each test. After the wear test, a Contour GT-K1 3D optical measurement system (Bruker Nano GmbH, Germany) was used to determine the worn volume of the coatings and stainless steel. The specific wear rate (k) of the coatings and stainless steel was calculated by the following equation (Ref 33):

$$k = V_w N^{-1} S^{-1}, \quad (\text{Eq 1})$$

where V_w is the worn volume, N is the applied load, and S is the sliding distance. Afterward, the worn surfaces and the debris from the coatings were examined by SEM/EDS

Table 1 Calculated temperatures and velocities of Al_2O_3 and $\text{Fe}_{66}\text{Cr}_{10}\text{Nb}_5\text{B}_{19}$ particles at an explosive charge of 50% and an $\text{O}_2/\text{C}_2\text{H}_2$ molar ratio of 1.1 for the particles with the diameter of 20, 30 and 40 μm

Size of a powder particle, μm	Al_2O_3		$\text{Fe}_{66}\text{Cr}_{10}\text{Nb}_5\text{B}_{19}$	
	Temperature, K	Velocity, m s^{-1}	Temperature, K	Velocity, m s^{-1}
20	786	771	1337	651
30	681	717	1443	567
40	917	631	1362	483

The melting temperature of the amorphous alloy was assumed to be 1442 K. The melting point of Al_2O_3 is 2319 K

Table 2 Concentration of Al_2O_3 , porosity, Vickers hardness and bonding strength of detonation coatings

Feedstock powder	Concentration of Al_2O_3 in coatings (estimated from SEM/optical images), vol.%	Porosity, %	Hardness, $\text{HV}_{1000\text{g}}$	Bonding strength, MPa
$\text{Fe}_{66}\text{Cr}_{10}\text{Nb}_5\text{B}_{19}$...	< 1	690 ± 30	125 ± 5
$\text{Fe}_{66}\text{Cr}_{10}\text{Nb}_5\text{B}_{19}$ -20 wt.% Al_2O_3 (33 vol.% Al_2O_3)	1.5 ± 2	≤ 2	655 ± 85	145 ± 15
$\text{Fe}_{66}\text{Cr}_{10}\text{Nb}_5\text{B}_{19}$ -40 wt.% Al_2O_3 (56 vol.% Al_2O_3)	4 ± 2	≤ 2	665 ± 80	140 ± 10
$\text{Fe}_{66}\text{Cr}_{10}\text{Nb}_5\text{B}_{19}$ -60 wt.% Al_2O_3 (74 vol.% Al_2O_3)	12 ± 1	≤ 3	660 ± 125	115 ± 15

Standard deviation is reported along with the average values

for gaining a better understanding of the wear mechanism of the coatings under dry sliding conditions.

The bonding strength of the coatings was determined by the pin test method (Ref 34–36). A conical pin with a flat end (1.5–1.8 mm in diameter) was placed into the conical hole of the matrix. After that, the end of the pin and the surface of the matrix were coated simultaneously. The bonding strength was determined by applying a force to the pin. The bonding strength was calculated by Eq 2:

$$\sigma = F (\pi r^2)^{-1}, \quad (\text{Eq 2})$$

where F is force and r is the radius of the flat end. The reported values of the bonding strength are averaged from five measurements. The standard deviation is also reported.

Results and Discussion

Characteristics of the Starting Powders and $\text{Fe}_{66}\text{Cr}_{10}\text{Nb}_5\text{B}_{19}\text{-Al}_2\text{O}_3$ Powder Mixtures

The XRD analysis revealed the predominance of an amorphous phase in the starting $\text{Fe}_{66}\text{Cr}_{10}\text{Nb}_5\text{B}_{19}$ powder

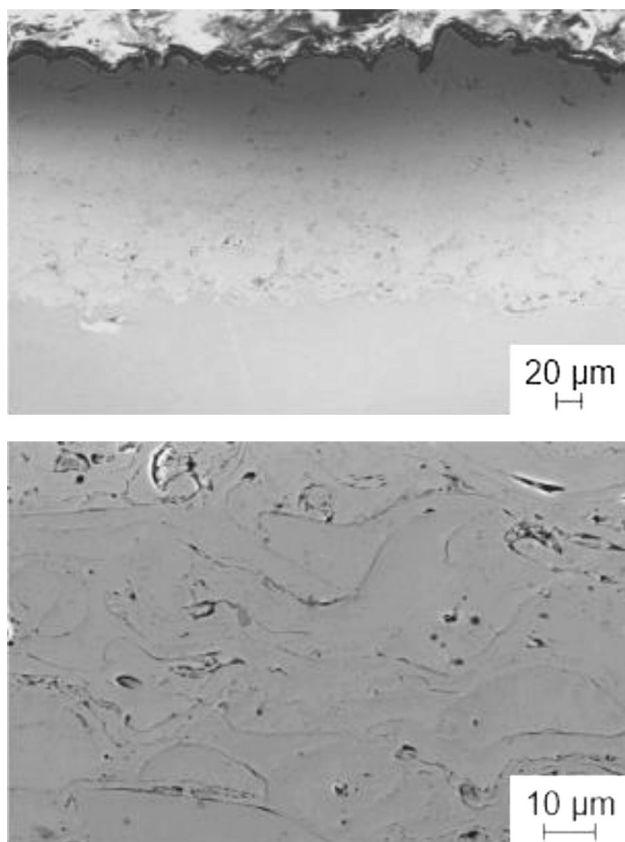


Fig. 3 Cross-sectional images of the $\text{Fe}_{66}\text{Cr}_{10}\text{Nb}_5\text{B}_{19}$ detonation coating (different magnifications). Micrographs were taken in the SE imaging mode

(Fig. 1a). The crystalline phase content in this powder was $\sim 5\%$. The glass transition T_g and crystallization T_x temperatures of the $\text{Fe}_{66}\text{Cr}_{10}\text{Nb}_5\text{B}_{19}$ alloy were determined in our previous work: $T_g = 794$ K, $T_x = 846$ K. A supercooled liquid region of 52 °C is an indicator of high glass-forming ability (Ref 13).

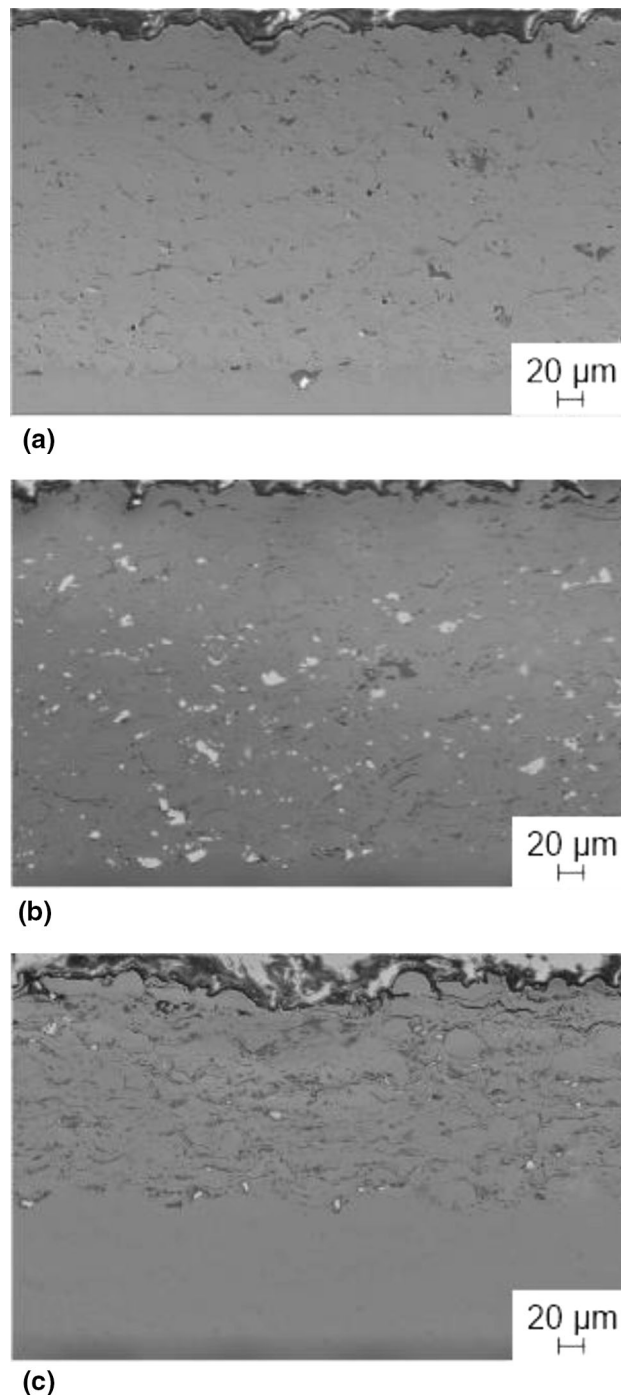


Fig. 4 Cross-sectional images of the detonation coatings obtained by spraying the powder mixtures with different Al_2O_3 concentrations: (a) 20 wt.% of Al_2O_3 ; (b) 40 wt.% of Al_2O_3 ; and (c) 60 wt.% of Al_2O_3 . Micrographs were taken by SEM in the SE imaging mode

SEM images of the $\text{Fe}_{66}\text{Cr}_{10}\text{Nb}_5\text{B}_{19}$ and alumina powders are shown in Fig. 1(b) and (c). The Fe-based alloy particles are spherical. This shape is characteristic of gas-atomized powders. The Al_2O_3 particles possess an irregular shape. Figure 2(a) shows the XRD patterns of the $\text{Fe}_{66}\text{Cr}_{10}\text{Nb}_5\text{B}_{19}\text{-Al}_2\text{O}_3$ feedstock powder mixtures. Narrow reflections in the patterns correspond to $\alpha\text{-Al}_2\text{O}_3$.

The calculated velocities and temperatures of the $\text{Fe}_{66}\text{Cr}_{10}\text{Nb}_5\text{B}_{19}$ and Al_2O_3 particles 20, 30 and 40 μm in size are presented in Table 1. The solidus temperature of the $\text{Fe}_{66}\text{Cr}_{10}\text{Nb}_5\text{B}_{19}$ alloy was determined as 1442 K (Ref 13). The melting point of alumina is 2319 K. A difference between the densities of the Fe-based alloy (7.58 g cm^{-3}) and alumina (3.96 g cm^{-3}) leads to differences in the particle velocities: The velocities of Al_2O_3 particles are higher than those of $\text{Fe}_{66}\text{Cr}_{10}\text{Nb}_5\text{B}_{19}$ particles. Alumina particles with a size of 20 μm , 30 μm and 40 μm reach velocities of 771, 717 and 631 m s^{-1} , respectively. Under the selected spraying conditions, the Fe-based 30- μm alloy particles start melting, while Al_2O_3 particles of the same size remain in the solid state (heated up to 681 K). Since

the Al_2O_3 particles are still solid, some particles can ricochet off the substrate or a previously deposited layer. The ricocheting events reduce the concentration of Al_2O_3 particles in the deposited coatings relative to the feedstock powder mixture. In addition, high velocities of brittle alumina particles create conditions for particles' crushing upon impact.

Microstructure and XRD Analysis of the Coatings

Figure 2(b) shows the XRD patterns of detonation coatings obtained by spraying the $\text{Fe}_{66}\text{Cr}_{10}\text{Nb}_5\text{B}_{19}$ powder and $\text{Fe}_{66}\text{Cr}_{10}\text{Nb}_5\text{B}_{19}\text{-Al}_2\text{O}_3$ mixtures. A halo in the patterns ($2\theta = 40\text{--}50^\circ$) indicates the presence of an amorphous phase in the composite coatings. The content of Al_2O_3 in the composite coatings was significantly lower than in the corresponding feedstock mixtures (Table 2). Because of a low concentration, it was rather difficult to detect Al_2O_3 in the coating by the XRD analysis. However, peaks of alumina were identified in the XRD pattern of the composite

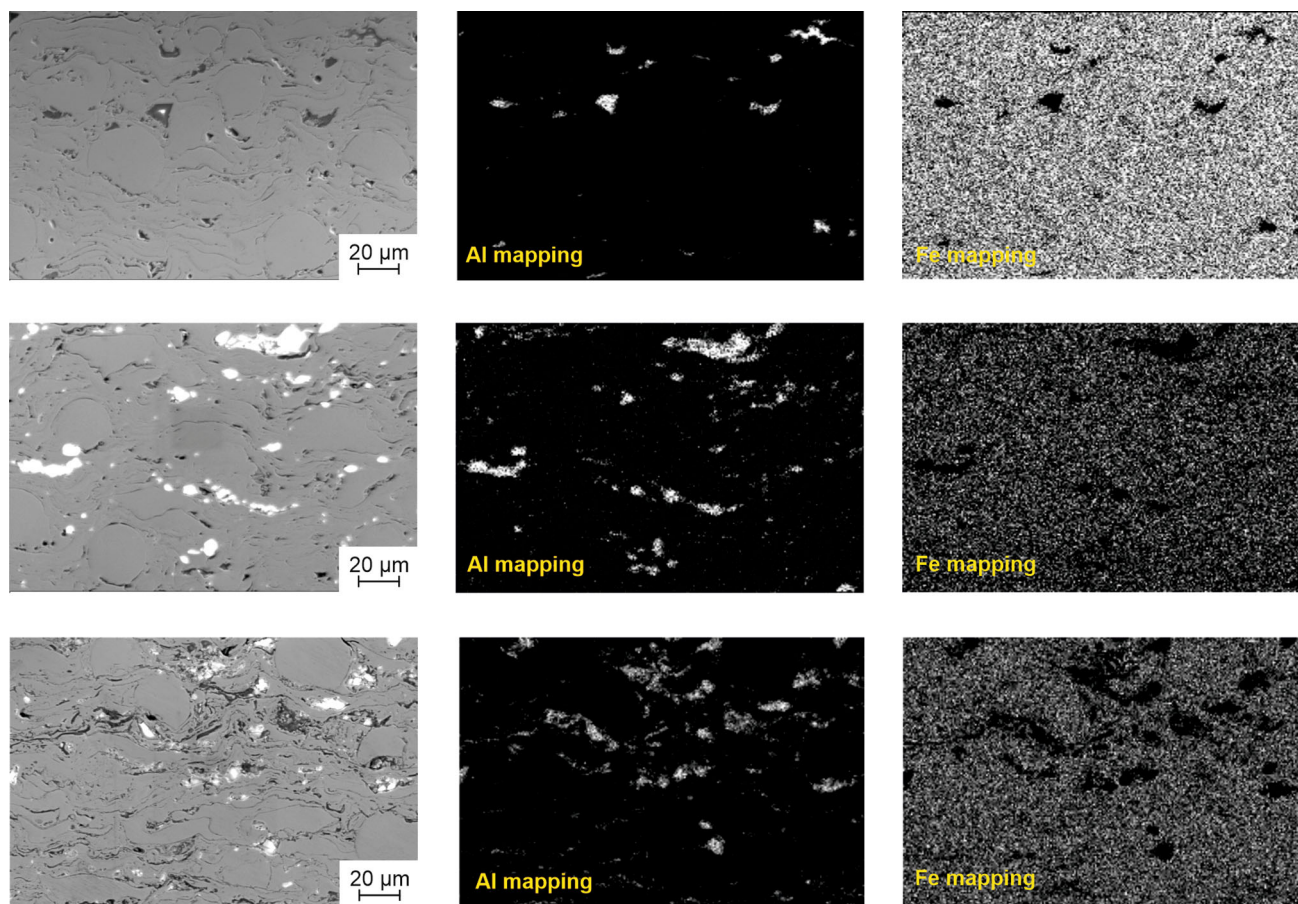
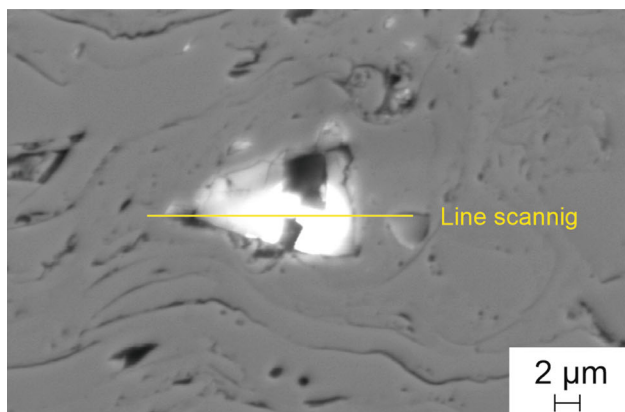


Fig. 5 SEM images and elemental Al and Fe distribution maps obtained from selected areas of the cross section of the composite coatings fabricated by spraying the powder mixture with 20 wt.%

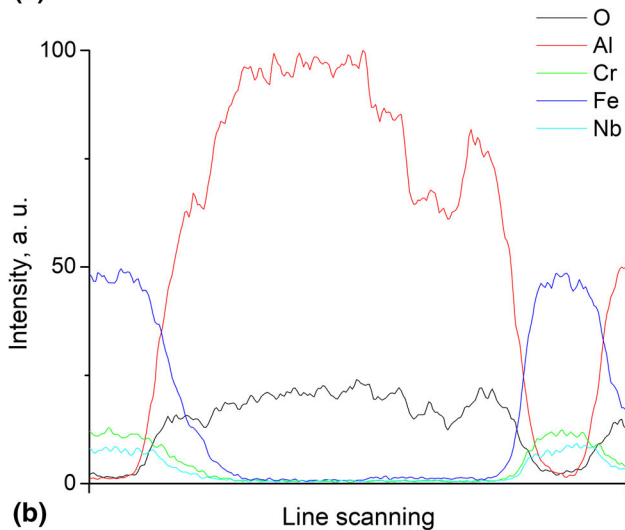
Al_2O_3 (a), 40 wt.% Al_2O_3 (b) and 60 wt.% Al_2O_3 (c). Micrographs were taken in the SE imaging mode

coating obtained from the feedstock powder mixture containing 60 wt.% of Al₂O₃.

The cross sections of the Al₂O₃-free coating and coatings modified with Al₂O₃ particles are shown in Fig. 3 and 4, respectively. The coatings exhibit a dense lamellar structure (the porosity is below 3%) typical of coatings obtained by thermal spray. The coatings demonstrate a greater number of pores and microcracks as the alumina content in the initial powder mixtures increases (Fig. 4a, b, and c). The detonation coatings were formed by molten (partially molten) particles of the Fe-based alloy and solid Al₂O₃ particles. It should be emphasized that effective densification upon deposition is favored when the sprayed particles reach the substrate in a partially molten state. A concentration of alumina of 60 wt.% in the feedstock powder corresponds to 74 vol.%. So, in this mixture, the content of Fe₆₆Cr₁₀Nb₅B₁₉ powder is only 26 vol.%. Such a low concentration of the alloy does not allow forming a defect-free coating. Fe and Al elemental maps are



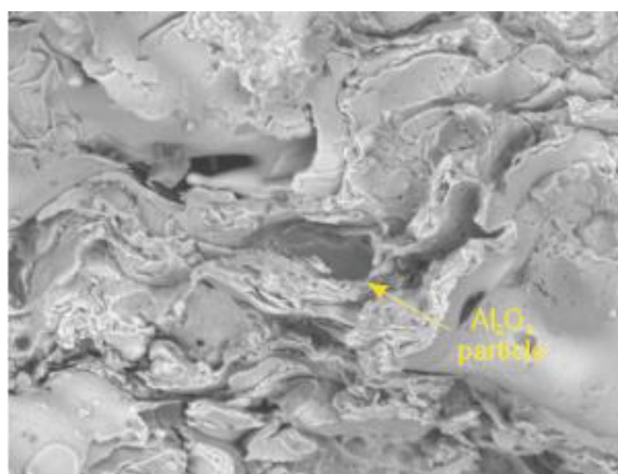
(a)



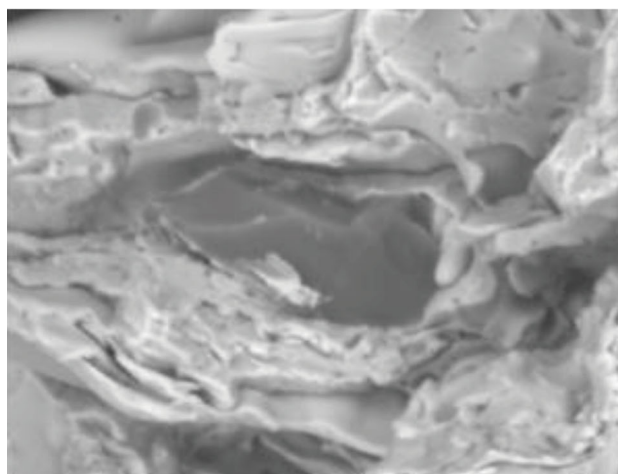
(b)

Fig. 6 SEM image of an area containing an Al₂O₃ particle (a) and the results of the EDS line scanning analysis (b). Micrograph was taken by SEM in the SE imaging mode

presented in Fig. 5. The maps were recorded from selected areas of the cross sections of the coatings with different alumina concentrations. A coating obtained from the mixture containing 20 wt.% of Al₂O₃ showed alumina inclusions in an amorphous matrix, but the number of particles was low (Fig. 5a). Spraying of mixtures containing 40 and 60 wt.% of alumina resulted in the formation of coatings with a relatively uniform distribution of the ceramic particles in an amorphous matrix (Fig. 5b and c). It is seen that, despite significant Al₂O₃ losses during spraying, the higher is the alumina content in the feedstock powder, the higher is the concentration of alumina in the coatings. As the Al₂O₃ particles crush upon impact onto the previously deposited layers, the inclusions in the coatings are smaller than the Al₂O₃ particles in the starting mixture.



(a)



(b)

Fig. 7 SEM image of the fracture surface of the detonation coating obtained by spraying the powder mixture containing 20 wt.% of Al₂O₃ (a) and a magnified image of an Al₂O₃ particle (b). Micrographs were taken in the BSE imaging mode

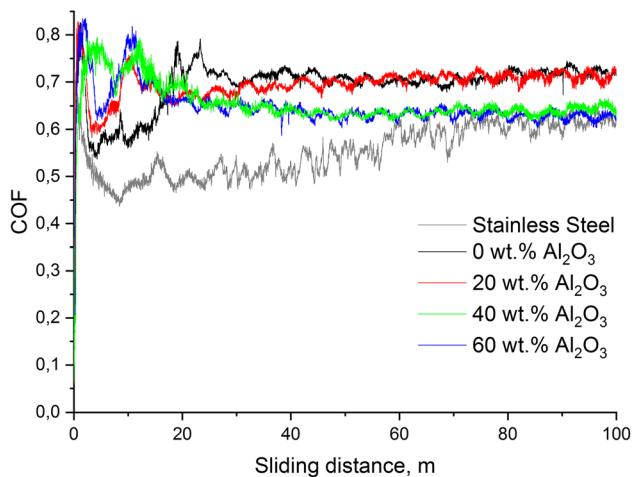


Fig. 8 The coefficient of friction versus the sliding distance. The plots were obtained for the stainless steel, Fe-based alloy coating and composite coatings (with different concentrations of Al_2O_3) sample under dry linearly reciprocating wear conditions under a normal load of 25 N. The concentration of Al_2O_3 in the feedstock powder mixtures is given on the plot

Table 3 Weight loss and specific wear rate of stainless steel, unmodified $\text{Fe}_{66}\text{Cr}_{10}\text{Nb}_5\text{B}_{19}$ coating and composite coatings

Material	Weight loss, mg	Specific wear rate ($10^{-5} \text{ mm}^3 \text{ N}^{-1} \text{ m}^{-1}$)
Stainless steel	3.6 ± 0.5	14.5 ± 0.5
$\text{Fe}_{66}\text{Cr}_{10}\text{Nb}_5\text{B}_{19}$	1.6 ± 0.4	2.6 ± 0.1
Coating obtained from $\text{Fe}_{66}\text{Cr}_{10}\text{Nb}_5\text{B}_{19}$ -20 wt.% of Al_2O_3 powder	1.2 ± 0.3	2.5 ± 0.4
Coating obtained from $\text{Fe}_{66}\text{Cr}_{10}\text{Nb}_5\text{B}_{19}$ -40 wt.% of Al_2O_3 powder	0.9 ± 0.3	3.1 ± 0.6
Coating obtained from $\text{Fe}_{66}\text{Cr}_{10}\text{Nb}_5\text{B}_{19}$ -60 wt.% of Al_2O_3 powder	2.4 ± 0.7	6.4 ± 0.9

The confidence intervals are given for the weight loss and specific wear rate (for a confidence level of 0.95)

The Al_2O_3 particles tend to form thin interlayers (with thicknesses of 5–10 μm) between the layers of an amorphous matrix (Fig. 5b and c).

As the temperature of the alumina particles is relatively low (Table 1), the cohesion between those and the amorphous matrix is weak. The reaction products at the amorphous matrix/alumina particle interface are absent, as concluded from results of the EDS line analysis (Fig. 6). Investigations of the fracture surface morphology of the coating obtained from the powder mixture containing 20 wt.% of Al_2O_3 confirm that the coating has a dense structure (Fig. 7). The alumina inclusions (indicated by

arrow in Fig. 7a) are located between the layers of an amorphous matrix. The amorphous alloy layers show high cohesion (to each other), as no signs of matrix delamination were found.

Hardness, Bonding Strength and Wear Resistance of the Coatings

The experimentally measured characteristics of the coatings (the concentration of Al_2O_3 , porosity, hardness, bonding strength to the substrate) are presented in Table 2. The hardness values of the composite and Al_2O_3 -free coatings did not differ significantly (considering the given values of standard deviation). The coatings in the studied series showed close values of bonding strength (130 MPa).

In Fig. 8, the coefficient of friction (COF) measured under dry reciprocating sliding conditions is plotted against the sliding distance for samples of the $\text{Fe}_{66}\text{Cr}_{10}\text{Nb}_5\text{B}_{19}$ coating, composite coatings and stainless steel. The wear process can be divided into a running-in stage and a steady-state stage. Fluctuations of COF at the steady-state stage are indicative of high wear rates. Detonation coatings showed relatively stable COFs at the steady-state stage, which was reached after a sliding distance of less than 30 m. The COF measured for the stainless steel sample was very unstable after a distance of 30 m: It increased from 0.5 to 0.6. (The average value was 0.56.) This can be attributed to a low hardness (~ 200 HV) and a high ductility of stainless steel.

At the steady-state stage, the unmodified coating and the composite coating produced from the mixture containing 20 wt.% of Al_2O_3 showed high COF; the average value was equal to 0.69 and 0.70, respectively. The average COF measured for coatings obtained from mixtures containing 40 and 60 wt.% of Al_2O_3 was 0.66 and 0.64, respectively. A reduction in COF is accompanied by an increase in the specific wear rate of the coatings, as shown in Table 3. This correlation was also reported in Zhang et al. (Ref 37) for spark plasma sintered materials.

The weight losses and specific wear rate of the $\text{Fe}_{66}\text{Cr}_{10}\text{Nb}_5\text{B}_{19}$ coating and composite coatings are given in Table 3. The $\text{Fe}_{66}\text{Cr}_{10}\text{Nb}_5\text{B}_{19}$ coating and composite coatings obtained from mixtures containing 20 and 40 wt.% of Al_2O_3 demonstrated close values of weight losses and specific wear rates. The coatings obtained from the powder mixture containing 60 wt.% of Al_2O_3 showed an increased specific wear rate. A general conclusion from the data presented in Table 3 is that the specific wear rate of the coatings is significantly lower than that of stainless steel.

Figure 9 shows the worn surface of composite coatings obtained from mixtures containing 20 and 60 wt.% of Al_2O_3 . The observed morphology of the worn surface is

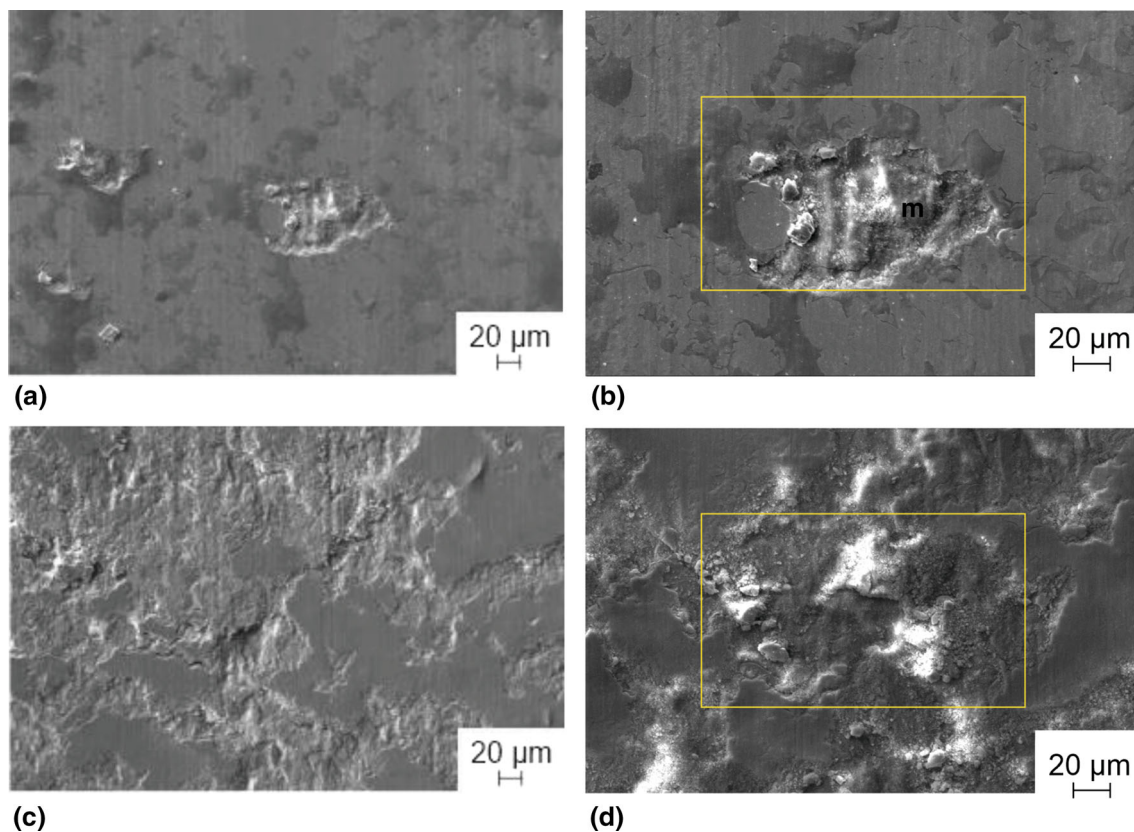


Fig. 9 Worn surfaces of the composite coatings fabricated from the powder mixtures containing (a, b) 20 wt.% Al_2O_3 ; (c, d) 60 wt.% Al_2O_3 . SEM images were obtained in the SE imaging mode at

different magnifications. Rectangles in (b) and (d) are the areas selected for the EDS analysis, the results of which are summarized in Fig. 10

typical of brittle fracture with detached lamellae (Ref 25, 38). It was shown that, under a high cyclic load, the coating lamellae may experience delamination (Ref 39). The detected lamellae indicate that fatigue wear is one of the main wear mechanisms of the composite coatings. The main reason for delamination could be a relatively low temperature developing in the coating-ball contact zone (not reaching T_g of the $\text{Fe}_{66}\text{Cr}_{10}\text{Nb}_5\text{B}_{19}$ alloy).

The number of delaminated lamellae was insignificant on the worn surface of the composite coating obtained from the powder mixture containing 20 wt.% Al_2O_3 (Fig. 9a). A larger number of delaminated particles on the worn surface of the coating obtained from the powder mixture containing 60 wt.% Al_2O_3 (Fig. 9c) can be explained by low cohesion between the ceramic and the matrix layers. The results of the elemental analysis of the worn surface prove this assumption (Fig. 10). As shown in Fig. 10(b), a higher concentration of aluminum was detected on the worn surface of the coating obtained from the powder mixture containing 60 wt.% Al_2O_3 (rectangle in Fig. 9d) than on the worn surface of the coating obtained from the mixture containing 20 wt.% Al_2O_3 (rectangle in Fig. 9b). The presence of tungsten on the worn surface was due to

material transfer from the WC-6Co ball to the sample surface. The transfer was possible because of the difference in the nature of chemical bonding in the coating material and WC (Ref 40).

During the wear tests, the delaminated particles did not leave the friction surface and acted as abrasive particles, contributing to microcutting (Fig. 9) and increasing the specific wear rate. The delaminated particles were of flaky shape and had diameters in the 20–80 μm range. Similar flaky debris was observed when a $\text{Fe}_{41}\text{Co}_7\text{Cr}_{15}\text{Mo}_{14}\text{C}_{15}\text{-B}_6\text{Y}_2$ bulk metallic glass and plasma-sprayed $\text{Fe}_{68.8}\text{C}_7\text{-Si}_{3.5}\text{B}_5\text{P}_{9.6}\text{Cr}_{2.1}\text{Mo}_2\text{Al}_2$ amorphous alloy coatings were tested (Ref 25, 41). During the wear tests, the energy dissipation causes heating of the contact zone and oxidation of the sliding surface. In addition to fatigue and abrasion wear by delaminated particles, oxidation wear can be suggested to play a role (Ref 42). However, the main wear mechanisms of the coatings tested in the present work are assumed to be fatigue and abrasion wear. It should be noted that the results of wear investigations are in agreement with refs. (Ref 22).

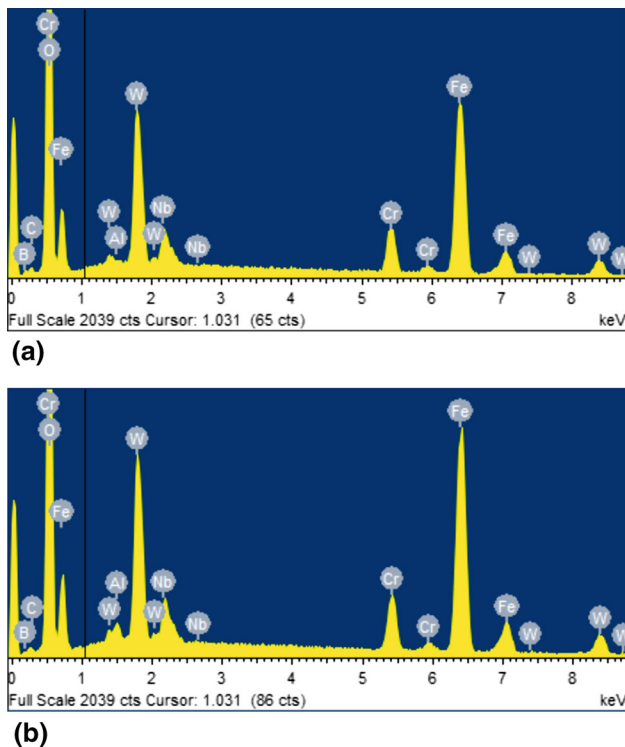


Fig. 10 Results of the elemental analysis of the worn surfaces of the composite coatings obtained from powder mixtures containing 20 wt.% Al_2O_3 (a) and 60 wt.% Al_2O_3 (b). The areas selected for the analysis are shown in Fig. 9

Conclusion

Composite coatings were fabricated by detonation spraying of $\text{Fe}_{66}\text{Cr}_{10}\text{Nb}_5\text{B}_{19}$ metallic glass-(20–60 wt.%) Al_2O_3 powder mixtures. The structural features and tribological properties of the coatings were investigated. The structural analysis has not revealed crystallization or oxidation of the amorphous matrix in the sprayed coatings. The alumina particles acquired high velocities during the detonation spraying process and crushed upon impact. Furthermore, the ricocheting events of the alumina particles did not allow maintaining the concentration of alumina in the coatings equal to that in the feedstock mixture. The specific wear rate of the coatings modified with 1.5 and 4 vol.% of Al_2O_3 was about one-fifth of the specific wear rate of stainless steel. Fatigue and abrasion appeared to be the dominant wear mechanisms of the composite coatings. Incorporating Al_2O_3 particles into an alloy matrix forming composite particles (agglomerates, composite feedstock) is possible by co-injection during gas atomization or through high-energy milling of the mixtures. The use of composite feedstock may be beneficial for reducing the intensity of ricocheting events upon deposition.

Acknowledgments This research was partially supported by the Russian Foundation for Basic Research, project 20-38-90069, and the NSTU Development Program, research project N^o C21-13. The analysis of samples was conducted at the Core Facility of NSTU “Structure, mechanical and physical properties of materials.”

References

1. S. Pang, T. Zhang, K. Asami and A. Inoue, Synthesis of Fe-Cr-Mo-C-B-P Bulk Metallic Glasses with High Corrosion Resistance, *Acta Mater.*, 2002, **50**, p 489–497. [https://doi.org/10.1016/S1359-6454\(01\)00366-4](https://doi.org/10.1016/S1359-6454(01)00366-4)
2. M. Iqbal, J.I. Akhter, H.F. Zhang and Z.Q. Hu, Synthesis and Characterization of Bulk Amorphous Steels, *J. Non-Cryst. Solids*, 2008, **354**, p 3284–3290. <https://doi.org/10.1016/j.jnoncrysol.2008.02.009>
3. A. Inoue, Stabilization of Metallic Supercooled Liquid and Bulk Amorphous Alloys, *Acta Mater.*, 2000, **48**, p 279–306. [https://doi.org/10.1016/S1359-6454\(99\)00300-6](https://doi.org/10.1016/S1359-6454(99)00300-6)
4. Y. Wang, Y.G. Zheng, W. Ke, W.H. Sun, W.L. Hou, X.C. Chang and J.Q. Wang, Slurry Erosion-Corrosion Behaviour of High-Velocity Oxy-Fuel (HVOF) Sprayed Fe-Based Amorphous Metallic Coatings for Marine Pump in Sand-Containing NaCl Solutions, *Corros. Sci.*, 2011, **53**, p 3177–3185. <https://doi.org/10.1016/j.corsci.2011.05.062>
5. L. Liu and C. Zhang, Fe-Based Amorphous Coatings: Structures and Properties, *Thin Solid Films*, 2014, **563**, p 70–86. <https://doi.org/10.1016/j.tsf.2013.08.029>
6. C. Zhang, K.C. Chan, Y. Wu and L. Liu, Pitting Initiation in Fe-Based Amorphous Coatings, *Acta Mater.*, 2012, **60**, p 4152–4159. <https://doi.org/10.1016/j.actamat.2012.04.005>
7. Y. Guo, G.Y. Koga, A.M. Jorge Jr., S. Savoie, R. Schulz, C.S. Kiminami, C. Bolfarini and W.J. Botta, Microstructural Investigation of Fe-Cr-Nb-B Amorphous/Nanocrystalline Coating Produced by HVOF, *Mater. Des.*, 2016, **111**, p 608–615. <https://doi.org/10.1016/j.matdes.2016.09.027>
8. Y. Zhou, G. Ma, H. Wang, G. Lu, Sh. Chen, H. Wang and M. Liu, Fabrication and Characterization of Supersonic Plasma Sprayed Fe-Based Amorphous Metallic Coatings, *Mater. Des.*, 2016, **110**, p 332–339. <https://doi.org/10.1016/j.matdes.2016.08.003>
9. Z. Zhou, L. Wang, F. Wang and Y. Liu, Formation and Corrosion Behavior of Fe-Based Amorphous Metallic Coatings Prepared by Detonation Gun Spraying, *Trans. Nonferrous Met. Soc. China*, 2009, **19**, p 634–638. [https://doi.org/10.1016/S1003-6326\(10\)60123-9](https://doi.org/10.1016/S1003-6326(10)60123-9)
10. P. Gargarella, A. Almeida, R. Vilar, C.R. Afonso, M. Peripolli, S. Rios and C.S. Kiminami, Formation of Fe-Based Glassy Matrix Composite Coatings by Laser Processing, *Surf. Coat. Technol.*, 2014, **240**, p 336–343. <https://doi.org/10.1016/j.surfcoat.2013.12.049>
11. L. Xie, Y.-M. Wang, X. Xiong and Z.-K. Chen, Comparison of Microstructure and Tribological Properties of Plasma, High Velocity Oxy-Fuel and Detonation Sprayed Coatings from an Iron-Based Powder, *Mater. Trans.*, 2018, **59**, p 1591–1595. <https://doi.org/10.2320/matertrans.M2018141>
12. D. Kuchumova, I.S. Batraev, N.Y. Cherkasova, D.K. Rybin, A.V. Ukhina, W.J. Botta, G.Y. Koga and A.M. Jorge Jr., The Influence of the $\text{O}_2/\text{C}_2\text{H}_2$ Ratio on the Structure and Properties of $\text{Fe}_{66}\text{Cr}_{10}\text{Nb}_5\text{B}_{19}$ Detonation Coatings, *Mater. Today Proc.*, 2020, **25**, p 384–386. <https://doi.org/10.1016/j.matpr.2019.12.098>
13. D. Kuchumova, I.S. Batraev, VYu. Ulianitsky, A.A. Shtertser, K.B. Gerasimov, A.V. Ukhina, N.V. Bulina, I.A. Bataev, G.Y. Koga, Y. Guo, W.J. Botta, H. Kato, T. Wada, B.B. Bokhonov, D.V. Dudina and A.M. Jorge Jr., Formation of Metallic Glass

- Coatings by Detonation Spraying of a Fe₆₆Cr₁₀Nb₅B₁₉ Powder, *Metals*, 2019, **9**, p 846. <https://doi.org/10.3390/met9080846>
14. J. Farmer, J.-S. Choi, C. Saw, J. Haslam, D. Day, P. Hailey and L. Aprigliano, Iron-Based Amorphous Metals: High-Performance Corrosion-Resistant Material Development, *Metall. Mater. Trans. A*, 2009, **40**, p 1289–1305. <https://doi.org/10.1007/s11661-008-9779-8>
 15. C. Zhang, H. Zhou and L. Liu, Laminar Fe-Based Amorphous Composite Coatings With Enhanced Bonding Strength and Impact Resistance, *Acta Mater.*, 2014, **72**, p 239–251. <https://doi.org/10.1016/j.actamat.2014.03.047>
 16. H. Zhou, C. Zhang, W. Wang, M. Yasir and L. Liu, Microstructure and Mechanical Properties of Fe-based Amorphous Composite Coatings Reinforced by Stainless Steel Powders, *J. Mater. Sci. Technol.*, 2015, **31**, p 43–47.
 17. P. Xu, C. Zhang, W. Wang and L. Liu, Pitting Mechanism in a Stainless Steel-Reinforced Fe-Based Amorphous Coating, *Electrochim. Acta*, 2016, **206**, p 61–69. <https://doi.org/10.1016/j.electacta.2016.04.130>
 18. G.Y. Koga, R. Schulz, S. Savoie, A.R.C. Nascimento, Y. Drolet, C. Bolfarini, C.S. Kiminami and W.J. Botta, Microstructure and Wear Behavior of Fe-Based Amorphous HVOF Coatings Produced from Commercial Precursors, *Surf. Coat. Technol.*, 2017, **309**, p 938–944. <https://doi.org/10.1016/j.surfcoat.2016.10.057>
 19. G.Y. Koga, A.M. Jorge Jr., V. Roche, R.P. Nogueira, R. Schulz, S. Savoie, A.K. Melle, C. Loable, C. Bolfarini, C.S. Kiminami and W.J. Botta, Production and Corrosion Resistance of Thermally Sprayed Fe-Based Amorphous Coatings from Mechanically Milled Feedstock Powders, *Metall. Mater. Trans. A*, 2018, **49**, p 4860–4870. <https://doi.org/10.1007/s11661-018-4785-y>
 20. G.Y. Koga, T. Ferreira, Y. Guo, D.D. Coimbra, A.M. Jorge Jr., C.S. Kiminami, C. Bolfarini and W.J. Botta, Challenges in Optimizing the Resistance to Corrosion and Wear of Amorphous Fe-Cr-Nb-B Alloy Containing Crystalline Phases, *J. Non-Cryst. Solids*, 2021, **555**, 120537. <https://doi.org/10.1016/j.jnoncrysol.2020.120537>
 21. G.Y. Koga, R.P. Nogueira, V. Roche, A.R. Yavari, A.K. Melle, J. Gallego, C. Bolfarini, C.S. Kiminami and W.J. Botta, Corrosion Properties of Fe-Cr-Nb-B Amorphous Alloys and Coatings, *Surf. Coat. Technol.*, 2014, **254**, p 238–243. <https://doi.org/10.1016/j.surfcoat.2014.06.022>
 22. W. Wang, C. Zhang, Z.-W. Zhang, Y.-C. Li, M. Yasir, H.-T. Wang and L. Liu, Toughening Fe-based Amorphous Coatings by Reinforcement of Amorphous Carbon, *Sci. Rep.*, 2017, **7**, p 4084. <https://doi.org/10.1038/s41598-017-04504-z>
 23. T. Terajima, F. Takeuchi, K. Nakata, S. Adachi, K. Nakashima and T. Igarashi, Composite Coating Containing WC/12Co Cermet and Fe-Based Metallic Glass Deposited by High-Velocity Oxygen Fuel Spraying, *J. Alloys Compd.*, 2010, **504**, p 288–291. <https://doi.org/10.1016/j.jallcom.2010.03.209>
 24. S. Yugeswaran, A. Kobayashi, K. Suresh and B. Subramanian, Characterization of Gas Tunnel Type Plasma Sprayed TiN Reinforced Fe-Based Metallic Glass Coatings, *J. Alloys Compd.*, 2013, **551**, p 168–175. <https://doi.org/10.1016/j.jallcom.2012.09.111>
 25. S. Yoon, J. Kim, B.D. Kim and C. Lee, Tribological Behavior of B₄C Reinforced Fe-Based Bulk Metallic Glass Composite Coating, *Surf. Coat. Technol.*, 2010, **205**, p 1962–1968. <https://doi.org/10.1016/j.surfcoat.2010.08.078>
 26. M. Yasir, C. Zhang, W. Wang, P. Xu and L. Liu, Wear Behaviors of Fe-Based Amorphous Composite Coatings Reinforced by Al₂O₃ Particles in Air and in NaCl Solution, *Mater. Des.*, 2015, **88**, p 207–213. <https://doi.org/10.1016/j.matdes.2015.08.142>
 27. M. Yasir, C. Zhang, W. Wang, Y. Jia and L. Liu, Enhancement of Impact Resistance of Fe-Based Amorphous Coating by Al₂O₃ Dispersion, *Mater. Lett.*, 2016, **171**, p 112–116. <https://doi.org/10.1016/j.matlet.2016.02.060>
 28. V. Ulianitsky, A. Shtertser, S. Zlobin and I. Smurov, Computer-Controlled Detonation Spraying: From Process Fundamentals Toward Advanced Applications, *J. Therm. Spray Technol.*, 2011, **20**, p 791–801. <https://doi.org/10.1007/s11666-011-9649-6>
 29. S. Batraev, E.S. Prokhorov and V.Y. Ul'yanitskii, Acceleration and Heating of Powder Particle by Gas Detonation Products in Channels with a Conical Passage, *Combust. Explos. Shock Waves*, 2014, **50**, p 315–322. <https://doi.org/10.1134/S0010508214030095>
 30. Yu. Nikolaev and M. Topchian, Analysis of Equilibrium Flows in Detonation Waves in Gases, *Combust. Explos. Shock Waves*, 1977, **13**, p 327–338. <https://doi.org/10.1007/BF01998461>
 31. T.P. Gavrilenko and Y.A. Nikolaev, Calculation of Detonation Gas Spraying, *Combust. Explos. Shock Waves*, 2007, **43**, p 724–731. <https://doi.org/10.1007/s10573-007-0098-y>
 32. ASTM G133-05, *Standard Test Method for Linearly Reciprocating Ball-on-Flat Sliding Wear*, Annual Book of ASTM Standards (ASTM, USA, 1995)
 33. A.L. Greer, K.L. Rutherford and I.M. Hutchings, Wear Resistance of Amorphous Alloys and Related Materials, *Int. Mater. Rev.*, 2002, **47**, p 87–112. <https://doi.org/10.1179/095066001225001067>
 34. V.Y. Ulianitsky, I.S. Batraev, A.A. Shtertser, D.V. Dudina, N.V. Bulina and I.A. Smurov, Detonation Spraying Behavior of Refractory Metals: Case Studies for Mo and Ta-Based Powders, *Adv. Powder Technol.*, 2018, **29**, p 1859–1864. <https://doi.org/10.1016/j.apt.2018.04.023>
 35. S. Schmidbauer, J. Hahn, F. Richter, B. Rother and H. Jehn, Adhesion of Metal Coatings on Ceramics Deposited by Different Techniques, *Surf. Coat. Technol.*, 1993, **59**, p 325–329. [https://doi.org/10.1016/0257-8972\(93\)90106-x](https://doi.org/10.1016/0257-8972(93)90106-x)
 36. H. Kasturi, T. Paul, S. Biswas, S.H. Alavi and S.P. Harimkar, Sliding Wear Behavior of Spark-Plasma-Sintered Fe-Based Amorphous Alloy Coatings on Cu-Ni Alloy, *J. Mater. Eng. Perform.*, 2018, **27**, p 3629–3635. <https://doi.org/10.1007/s11665-018-3470-z>
 37. C. Zhang, L. Liu, K.C. Chan, Q. Chen and C.Y. Tang, Wear Behavior of HVOF-Sprayed Fe-Based Amorphous Coatings, *Intermetallics*, 2012, **29**, p 80–85. <https://doi.org/10.1016/j.intermet.2012.05.004>
 38. D. Huang, R. Li, L. Huang, V. Ji and T. Zhang, Fretting Wear Behavior of Bulk Amorphous Steel, *Intermetallics*, 2011, **19**, p 1385–1389. <https://doi.org/10.1016/j.intermet.2011.04.014>
 39. D.J. Branagan, W.D. Swank, D.C. Haggard and J.R. Fincke, Wear-Resistant Amorphous and Nanocomposite Steel Coatings, *Metall. Mater. Trans. A*, 2001, **32**, p 2615–2621. <https://doi.org/10.1007/s11661-001-0051-8>
 40. C.J. Li and A. Ohmori, Relationships Between the Microstructure and Properties of Thermally Sprayed Deposits, *J. Therm. Spray Technol.*, 2002, **11**, p 365–374. <https://doi.org/10.1361/105996302770348754>
 41. T.F.J. Quinn, Review of Oxidational Wear Part II: Recent Developments and Future Trends in Oxidational Wear Research, *Tribol. Int.*, 1983, **16**, p 257–271. [https://doi.org/10.1016/0301-679X\(83\)90086-5](https://doi.org/10.1016/0301-679X(83)90086-5)
 42. H. Wu, X. Lan, Y. Liu, F. Li, W. Zhang, Z. Chen and H. Zeng, Fabrication, Tribological and Corrosion Behaviors of Detonation Gun Sprayed Fe-Based Metallic Glass Coating, *Trans. Nonferrous Met. Soc. China*, 2011, **26**, p 1629–1637. [https://doi.org/10.1016/S1003-6326\(16\)64271-1](https://doi.org/10.1016/S1003-6326(16)64271-1)